LAWRENCE
LIVERMORE
NATIONAL
LABORATORY

LLNL-JRNL-716802

Determination of the laser intensity applied to a Ta witness plate from the measured X-ray signal using a pulsed micro-channel plate detector

L. A. Pickworth, M. D. Rosen, M. B. Schneider, D. E. Hinkel, L. R. Benedetti , R. L. Kauffmann, S. S. Wu

January 5, 2017

High Energy Density Physics

Disclaimer

Determination of the laser intensity applied to a Ta witness plate from the measured X-ray signal using a pulsed micro-channel plate detector

L. A. Pickworth, M. D. Rosen, M. B. Schneider, D. E. Hinkel, L. R. Benedetti, R. L. Kauffman, S. S. Wu

Lawrence Livermore National Laboratory, Livermore, CA, USA

Abstract

The laser intensity distribution at the surface of a high-Z material, such as Ta, can be deduced from imaging the self-emission of the produced x-ray spot using suitable calibration data. This paper presents a calibration method which uses the measured x-ray emissions from laser spots of different intensities hitting a Ta witness plate. The x-ray emission is measured with a micro-channel plate (MCP) based x-ray framing camera plus filters. Data from different positions on one MCP strip or from different MCP assemblies are normalized to each other using a standard candle laser beam spot at $\sim 1 \times 10^{14}$ W/cm^2 intensity. The distribution of the resulting dataset agrees with results from a pseudo spectroscopic model for laser intensities between 4 and 15×10^{13} W/cm^2. The model is then used to determine the absolute scaling factor between the experimental results from assemblies using two different x-ray filters. The data and model method also allows unique calibration factors for each MCP system and each MCP gain to be compared. We also present simulation results investigating alternate witness plate materials (Ag, Eu and Au).

Keywords: Plasma Diagnostics; Laser beam spot; X-ray imaging; Beam intensity profile

1. Introduction

High intensity lasers provide a means to investigate exotic states of matter and laboratory fusion experiments. Determination of the laser energy delivered to the target surface can become a complex problem when gas and plasma are in the path of the beam. For high intensity ($>2 \times 10^{13}$ W/cm^2) laser beams the far-field intensity is most often inferred from calculations using the delivered energy, the pulse shape of the laser, and the expected spatial profile at the surface of interest, which is often situated close to the focus of the beam[1]. When a gas or plasma is in the beam path, scattering, filamentation, absorption and other power loss mechanisms must be accounted for when estimating the delivered power. If multiple laser beams are interacting, cross beam energy transfer (CBET)[2, 3] can also come into play. It is beneficial in complex geometries to have a direct measure of the power at the surface of interest, and for high intensity lasers the abundant x-ray self-emission can provide such a witness.

We are interested in applying a direct measurement technique to visualizing the laser beams that propagate to the waist of an indirect drive Inertial Confinement Fusion (ICF) hohlraum[4] at the National Ignition Facility (NIF)[5]. The hohlraum is shown in Figure 1a. In this configuration, 192 beams grouped into 48 quads of two outer cones (16 quads, 64 beams each in 50° and 44.5° cones) and two inner cones (8 quads, 32 beams each in 30° and 23.5° cones) heat a cylindrical Au hohlraum that may be filled with low-Z gas, e.g He. The outer beams hit the hohlraum wall near the Laser Entrance Holes (LEH) and the inner beams hit near the center (or waist) of the hohlraum.

In order to map the intensity profile of the inner quads near the waist, we have designed a shortened gas filled hohlraum target, with a length of $\sim 1/4$ to $1/3$ of the standard length, which we call the 'quartraum'[6, 7] . The quartraum is shown in Figure 1b. The 96 beams from the lower half of the NIF chamber enter the single LEH; the quartraum is long enough so that the outer beams terminate on the wall but the inner beams escape and two inner quads hit a flat 'witness plate' at almost normal incidence. The plate is positioned outside of the quartraum at approximately the location of the waist of the hohlraum. The quartraum is designed to preserve the plasma conditions in the LEH region and replicate the plasma conditions the inner beams must traverse before hitting the hohlraum wall. The quartraum experiment laser drive was designed to mimic the 'picket'[8]

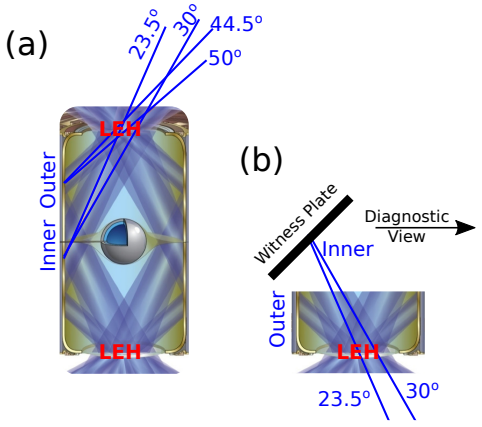

Figure 1: (a) Diagram of the ICF hohlraum showing the inner and outer beam intersections on the wall. The lasers drive x-ray emission of the Au hohlraum which ablates the outer surface of the capsule, imploding the capsule inner surface at a very high velocity. (b) the quartraum target[6, 7] is a shortened hohlraum which preserves the interaction of one half of the NIF beams in the region of the lower laser entrance hole (LEH). The inner beams escape the quartraum and 2 sample 'quads' (a quad is 4 beams originating from the same port in the NIF chamber) are captured on a witness plate.

of a High Foot [9] ICF laser drive. There is significant CBET during the picket and we desired to test the hypothesis that the CBET was not uniform across the laser beam cross-section. The laser intensity hitting the witness plate was expected to be $\sim 1 \times 10^{14}$ W/cm^2. Images of the x-ray emission from the inner beam laser spots on the plate are taken ~1.3 ns after the beams first hit the plate using a time resolved detector with 100 ps integration. This allows flexibility in the experimental platform to observe time dependent changes in the laser beam intensity profile.

This paper presents the calibration required to infer the laser intensity spatial distribution on the witness plate from the x-ray self-emission. We achieve this goal in a separate calibration experiment by imaging laser spots with different known intensities onto the witness plate. We then compare the measurements with simulations and find that the experimental results from the calibration experiment closely follow the simulated relationship of laser intensity and x-ray emission. We perform the experimental calibration for three separate micro-channel plate (MCP) based x-ray framing camera detectors. The technique itself is self-calibrating, and does not require accurate knowledge of plasma conditions, though agreement to the simulations presented here helps build our understanding on the behavior of the observed x-ray emission and validates extension outside of the exact experimental configurations described in this paper.

While the geometry and conditions for the calibration described here are closely matched to the quartraum experiment, it is significant to note that the technique is readily applicable to other experimental conditions of interest to the high energy density physics community[10].

2. Calibration Experiment

The calibration experiment consists of a tilted witness plate with a number of separate laser beam spots incident on its surface, as shown in Figure 2a. The witness plate target has two separate 25 μm thick Ta witness plates at 45° to the horizontal. Each laser spot consists of two overlapped beams from the same quad, (in the quartraum experiment the four beams from one single quad will overlap to create a beam spot). The witness plate is almost normal to the beam propagation direction so the x-ray spot is elliptical (~1.8 mm × 1.4 mm FWHM) as the NIF phase plates produce an elliptical spot near focus[11]. Three well separated laser spots are produced on each witness plate by six independently pointed laser beams. One laser spot visible to the MCP will be at an intensity of $\sim 1 \times 10^{14}$ W/cm^2. The upper witness plate has two laser beam spots that partially overlap (see Figure 2b) to allow the investigation of a adjacent laser intensity region being different (the central region of this beam spot is twice as bright as the outer region, forming a 2:1 intensity profile).

The x-ray emission produced by the laser beam spots is imaged using a pinhole camera attached to a time resolved MCP[13, 14, 15] x-ray detector, see Figure 3. The pinhole camera views the front (laser) side of the witness plate at 45° to the witness plate normal, as shown in Figure 3b. We investigated a range of laser intensities from 3.9 to $\sim 14.3 \times 10^{13}$ W/cm^2, which was controlled by the delivered laser pulse, shown in Figure 2c. This laser pulse was designed to mimic the time evolution of the laser intensity on the quartraum witness plate accounting for CBET, absorption and the time to burn through the windows that hold the gas in the quartraum. Figure 2d shows the expected laser intensity distributions at the witness plate for one of the laser spots in the calibration experiment, which traverses chamber vacuum before intersecting the witness plate.

The laser spots are imaged by a 2× magnification pinhole camera, shown in Figure 3. The pinholes are 15 μm in diameter and located 190 mm from the witness plate. The detection region of the camera is two co-timed strips ~35 mm ×15 mm. The four pinholes produce four separate images. We differentially filtered

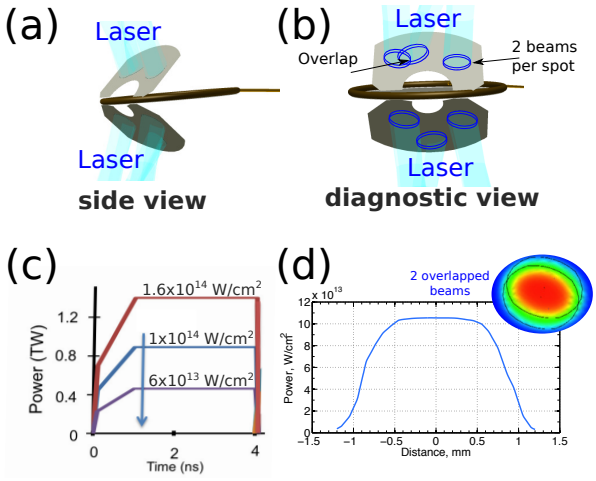

Figure 2: The witness plate experiment; (a) and (b) show the witness plate calibration target with intersecting laser beams. The beams arrive at the target near best focus. The upper and lower plates are tilted 45° from the view of the diagnostic, to match the plate shown for the Quartraum target (Figure 1b). (c) The laser pulse shape. The peak power is varied between separate beam spots to view different intensities on the same target. (d) Predicted spatial intensity variation in the applied laser intensity as estimated by VISRAD[12] (image) and a line-out through the center of the VISRAD image.

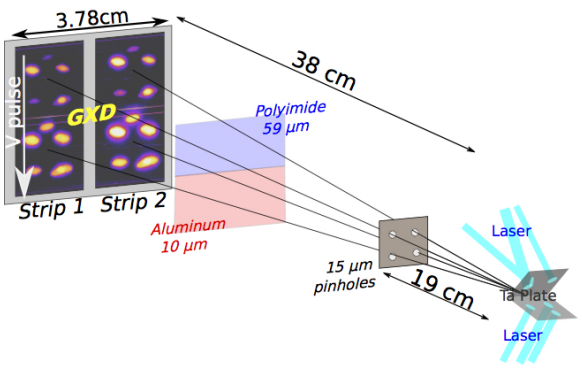

Figure 3: A schematic showing the experimental set up. A set of four pinholes produces four images with magnification 2× on a two-strip microchannel plate (MCP) detector. Each image is filtered with either a 59 μm thick polyimide or 10 μm thick Al filter such that each strip contains one image from each filter. The two strips have different gains and are co-timed.

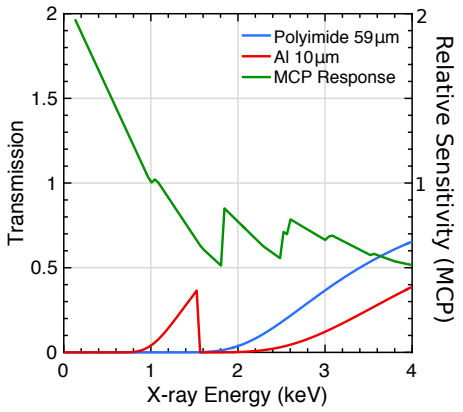

Figure 4: Plots vs. x-ray energy of the transmission of the thin polyimide (blue) and aluminum (red) filters (Figure 3) and the relative sensitivity of the MCP[16] (green), from the normalized QE of the MCP at 1 keV. At 1 keV the MCP has a QE of 556.5 electrons/ photon for a DC bias of 50 V.

the images so that the spectral content of the images would be sensitive to different parts of the laser spot x-ray spectrum. This is achieved by using thin foils. We used 10 μm aluminum to image x-rays at ~1.5 keV and 59 μm polyimide, to image x-rays >2 keV. The detector was configured to produce two co-timed images at 1.5 keV and two images at >2 keV. The transmission function of the filters is shown in Figure 4.

Using the measured brightness of the x-ray images on the MCP and the known intensity of each beam spot at the witness plate we are able to create an experimental calibration linking x-ray brightness to the delivered laser intensity. This calibration is unique to the specific MCP assembly used but data from different assemblies can be normalized using a standard candle laser beam spot which is chosen to be 1×10^{14} W/cm^2. This method enables different assemblies to be calibrated to each other. This work describes the calibration of three separate MCP assemblies using a witness plate with known laser intensity pattern.

The x-ray detection medium is the leaded-glass of the MCP[13]. An x-ray photon absorbed in the MCP may be converted to an electron that may then be amplified if an accelerating voltage is present. The electrons exit and are incident on a phosphor that converts the electrons into visible light. The visible light is coupled to a CCD detector or film by an optical fiber block. The CCD read out or scanned film is digitized to detector counts that are approximately proportional to the number of electrons incident on the phosphor.

The spatial resolution of the detector is ~50 μm,

which gives a experimental resolution at the target of ~30 μm from the quadrature additions of the pinhole, diffraction and detector resolutions.

Temporal resolution is achieved by applying voltage to the MCP as a pulse, forming a moving shutter, giving ~100 ps exposure at any single point on the strip. The pulse moves at ~150 mm/ns.

Gain is a highly non-linear function of the amplitude and shape of the voltage pulse. This results in no two assemblies of the MCP detectors being truly identical in their response for a given experimental set up[17].

The amplitude of the voltage pulse decreases as the pulse moves across the strip of the MCP because of resistive effects. Due to the sensitive relationship of the gain to voltage, this results in a gain variation from the start of the strip to the end. This effect depends on the relative timing of all the strips on the detector and the bias voltage used to set the gain[15]. The DC bias voltage used in these experiments was 50 V, which is the highest gain setting for the MCP.

The effect of the gain variation along the strip can be removed during data analysis if there exists a flat field for the detector taken with the same timing and bias configuration[18]. We did not have a flat field for the experiments discussed in this paper as the existing flat fields are for detector inter strip timing and bias used in ICF implosion imaging, which differs from the high gain and co-timed setup needed for the quartraum experiment. The data can be corrected for the relative gain variation between the separate strips because images are taken at same time with the same filters. However, we are limited in our ability to make an absolute measurement of x-ray flux by the detector and thus cannot account for the gain variation from beginning to the end of the strip because the images are on different filters. However the direct calibration technique of the three detectors in this paper does not require a flat filed as long as the detectors are used in the same timing and bias configurations as the calibration experiment.

The quantum efficiency (QE) of the MCP is defined as the number of electrons produced per incident photon. The QE depends on the material composition of the MCP. The QE of similar MCP detectors was measured by Rochau et al. (2006)[16] and shows a number of abrupt edges in the photon energy range of 1-5 keV. The relative response of the MCP is shown in Figure 4 alongside the transmission of the filters used. This sensitivity curve is a valid approximation for the response of the NIF MCP detectors, though there may exist small variations in the percent of the absorbing materials that contribute to the edges in this range.

All the data from a given filter can be normalized using the standard candle beam spot at (or close to) 1×10^{14} W/cm^2. The shape of the resulting distribution of data points will be compared to results from a pseudo spectroscopic model whose results are post-processed through the response of the filters in addition to the MCP assembly. The model is discussed in the next section and the data analysis is discussed in Section 4.

3. Simulations

To determine the expected x-ray signal from the witness plate we performed detailed 2D simulations using the radiation-hydrodynamics code LASNEX[19]. The physics model is the non-local thermodynamic equilibrium (NLTE) detailed configuration accounting (DCA) atomic physics[20] with a non-local electron heat package[21]. Together these two packages constitute the high flux model[22] used to date in NIF ICF ignition design[23], and analysis[24].

Figure 5a, inset, shows the geometry for the simulation of the calibration experiment. The simulated target consists of 0.3 μm thick Ta with a backing of 25 μm of plastic (CH) and is vertical along the y-axis with the Ta side facing the laser beam which is incident from the right. In the experiment the target is 25 μm of Ta in thickness. We simulated plastic-backed Ta to allow for the possible extension of the technique to viewing the beam from the rear of the witness plate. This target configuration has no effect on the emission from the front side of the plate. At the time of interest, 1.3 ns into the laser pulse, the 0.3 μm Ta in the simulation has not burnt through. The applied laser profile is an elliptical spot with major/minor axes of 640 and 880 μm. The profile is a 5.1 supergaussian.

Figure 5a and b are maps of electron temperature (T_e) and contours of electron density (n/n_c in black) and laser intensity (magenta) at 1.3 ns. Since the quartraum will radiate soft x-rays onto the witness plate surface, we apply an approximate 80 eV black body radiative flux onto the witness plate prior to and during the arrival of the laser pulse (in the simulation this is incident on the plate from 50 ps, applied as a field across the whole plate). This is an estimate based on the simulated radiation temperature from the quartraum and the distance of the witness plate. Figure 5a shows this run. Since the witness plate calibration experiment (Figure 2) does not experience such an external radiative flux, we re-ran the calculation, dropping that radiative flux by a factor of 10,000 to understand the effect on our simulated results; Figure 5b is from this run. There is very little difference between these two runs because the laser is

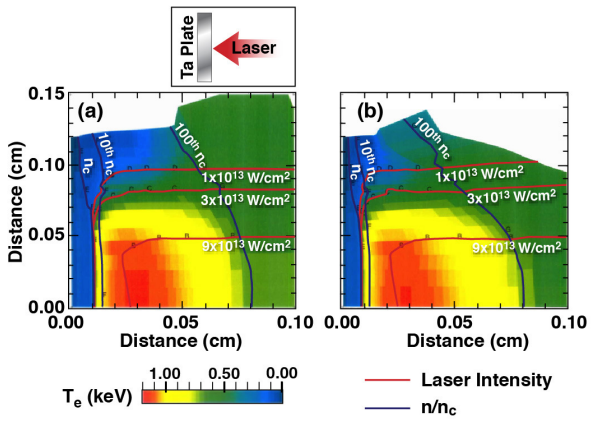

Figure 5: Simulation of the laser interaction with the Ta witness plate at 1.3 ns. Inset is a diagram of the simulation setup (a) the electron temperature, T_e, map with an 80 eV black body external radiation field, in addition to the laser. (b) T_e map with an 8 eV black body external radiation field. Black lines indicate the electron density contours, n/n_c (1,0.1,0.01) and laser irradiance contours are in magenta (9, 3 and 1×10^{13} W/cm^2). The comparison shows the external radiation field has little effect on the T_e map and density contour locations.

the main heating mechanism producing the hard x-rays that make up the witness plate self emission that we use to build the calibration.

The x-ray self-emission intensity is weighted by $n^2 T_e$ [25]. This means it is localized near the $n/n_c = 0.1$ contour in Figure 5a,b which is at z ~125 μm or 100 μm from the original surface of the witness plate at 25 μm. Given the size of the spot (640 and 880 μm in major/minor radius) this is still nearly planar, despite the radiative preheat.

We estimate that the laser intensity profile at the target surface can be deduced from our measurements if the $(n_c/10)$ surface, which is where the emitting surface is localized, remains within 500 μm of the initial surface of the witness plate. This limitation is primarily due to diagnostic viewing angle and proximity of the front of the witness plate to the quartraum in addition to our aim to sample the laser beam profile close to the original plate surface location. During the evolution of the plasma on the plate the emitting surface will move away from the initial position of the witness plate surface at the sound speed of the plasma (~100-150 μm/ns). This places an upper limit on the length of the laser pulse for which this technique, as described in this paper, could be applied of ~3 to 5 ns, dependent on the T_e in the plasma created at the plate and the intensity of the beam. For alternate target geometries this technique can be applied as long as the M-shell emission remains localized in the target surface plasma.

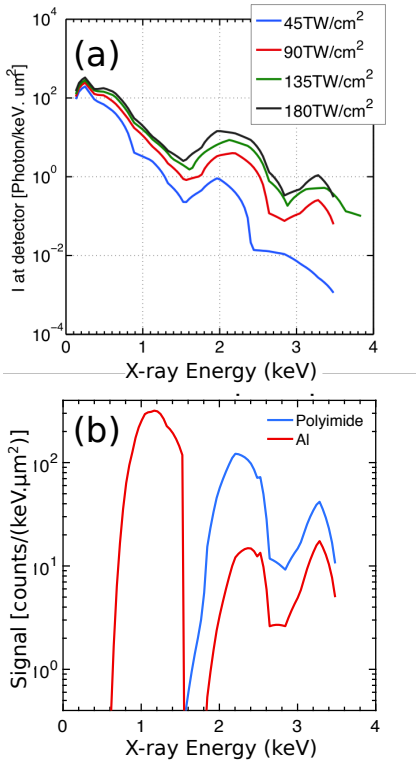

Figure 6: Simulated spectra from the whole applied laser beam spot at 1.3 ns in the laser pulse. The 'bumps'' (near ~2 keV and ~3.3 keV) correspond to M-shell emission, the lower energy are n=4 to 3 transitions, higher energy are n=5 to 3 transitions[26]. (a) for 4 applied laser intensities. (b) Detected spectra for laser intensity 9×10^{13} W/cm^2 using the detector sensitivity and the transmission of the thin foil.

The simulated x-ray spectra from the Ta witness plate at 1.3 ns are shown in Figure 6a. Figure 6b shows the x-ray spectra transmitted through the filters and attenuated by the MCP energy dependent QE function, Figure 4. This shows the spectral sensitivity of the two channels. Table 1 gives the integrated power in 4π for the total emission and through the two filters without the MCP QE function for reference.

I_L, (W/cm^2)	Total x-ray radiance, (GW)	Al, (GW)	Polyimide, (GW)
4.5×10^{13}	570.5	4.5	1.3
9×10^{13}	1145.2	16.2	17.1
13.5×10^{13}	1720.2	30.4	44.2
18×10^{13}	2289.4	40.7	71

Table 1: X-ray simulated integrated total power (GW) in 4π both without and through the thin foil filters, not including the effect of the MCP, emitted from the whole simulated x-ray spot.

Applying the filter response, QE (Figure 4b) of the detector and the geometry to the simulated spectra (Figure 6a) gives the expected x-ray signal per unit area in the detector, I_x . The MCP response is modeled here as a photon counter, not a calorimeter.

$$I_x = \frac{d\Omega \Delta t}{eAM^2} \int_0^\infty \frac{S(E) \cdot T(E) \cdot QE(E)}{E} dE \qquad (1)$$

Where I_x is in detector counts/μm^2, or electrons produced by the MCP per μm^2. E is the photon energy in keV, $d\Omega$ is the solid angle of the imaging system given by $d\Omega = \frac{\pi r^2}{z^2}$, where r is the radius of the pinhole and z is the distance of the pinhole from the target. The solid angle of the imaging system used is 2.04×10^{-8}sr. Δt is the time integration period of the detector (100 ps), A is the area of the beam spot ($\pi(640 \times 880)$) in μm^2, M is the magnification of the imaging system (2×). S is the simulated spectrum in W/keV.sr, from the whole beam spot. T is the transmission of the filter and QE is the quantum efficiency of the detector in electrons/photon at the experimental DC bias voltage, Figure 4. e is the electron charge in C, required to convert the spectrum to a photon flux.

The calculated detector signal vs. applied laser intensity is shown in the log-log plot in Figure 7. The calculated simulated signal is plotted on a log-log plot to illustrate the regions that partially follow a power law relationship. For both filters, the signals appear to fall into two approximate regions, marked with lines in Figure 7. In each region, the signal follows a power law, $I_x = aI_L{}^b$ but b, the exponent is different, and the values are given in Figure 7. For completeness Figure 7 includes results from both 2D simulations (circles) and a 1D simulation (triangles).

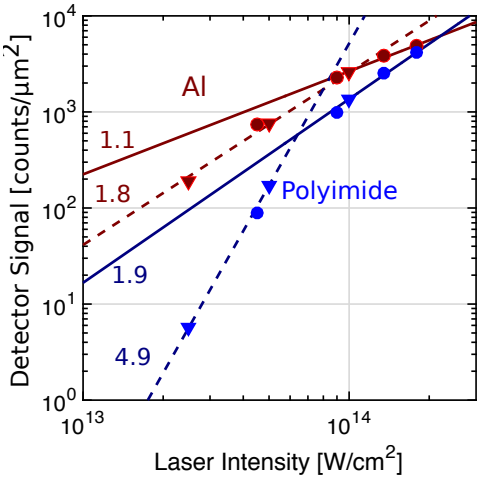

Figure 7: The simulated detector signal vs. applied laser intensity for the Ta witness plate is obtained by integrating the attenuated emission (as shown in Figure 6b) for each laser intensity. The plot is log-log and shows the Al channel in red, and the polyimide channel in blue. The straight lines are power laws with the exponent indicated on the figure, to guide the reading of the figure. The results include 2D simulations (circles) and 1D simulations (triangles).

The 1D simulation output is post processed to give the emitted power per solid angle detected through the experimental filters. It does not account for the response of the x-ray detector. In order to compare the 1D values to the processed 2D simulation, the 1D simulation values are scaled to the 2D output using the data point closest to 1×10^{14} W/cm^2. The 2D and 1D data points show agreement near 5×10^{13} W/cm^2 indicating the problem is effectively 1D in nature.

4. Experimental results and comparison to simulation

Figure 8 shows the calibration experiment x-ray images of the applied laser spots and the calculated laser intensity at the target found using VISRAD[12] with the NIF phase plates[27] and experimentally delivered power to the witness plate. Near to the focal point of the beam this gives and accurate estimation of the laser intensity dominated by the 1.5% uncertainty in the laser delivered power. Comparison of the images shows that the x-ray signal from both filters follows the broad laser intensity shape, but both x-ray beam spots do not follow

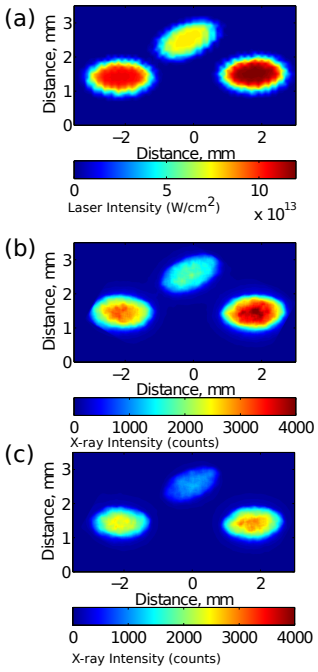

Figure 8: (a) shows the predicted laser intensity, predicted using VISRAD and measured experimental laser power (~1.5% uncertainty), incident on the witness plate viewed at 45° to the plate normal. (b) shows the recorded emission from the experiment on the Al filter channel and (c) shows the x-ray emission recorded on the polyimide filter channel.

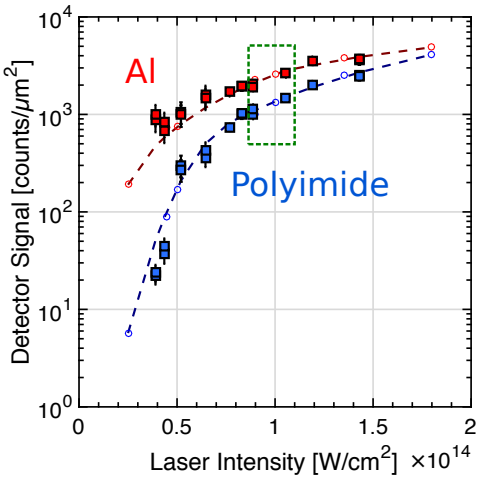

Figure 9: The calibration experiment was performed twice; yielding 34 distinct data points on 3 separate x-ray detectors. The Al channel is shown in red and the polyimide channel in blue. The data is matched to the simulated response (dashed lines and open circle markers) by scaling the data points closest to 1×10^{14} W/cm^2(marked in dashed green box). The simulation matches the data in x-ray emission within the 10% error bars in the regions that were not constrained above 0.6×10^{14} W/cm^2, below this laser intensity the experimental data is reported with a 20% error bar.

a super-Gaussian laser intensity profile, which the laser does follow. As expected from the simulation, in this case the measured x-ray signal is reduced on the polyimide filter.

The raw x-ray images are processed by analyzing a small region in the center of each x-ray spot. The x-ray background is subtracted and then an average signal (counts per resolution region) is calculated for each x-ray spot from a small area in its center where the laser intensity is known to be flat, as predicted by VISRAD. This number is converted to counts/μm^2 after normalization to a 15 μm pinhole diameter. The detector yields two sets of polyimide and aluminum images on separate, co-timed strips of the MCP. Each dataset from one MCP build is then scaled to the simulation using the data point closest to a laser intensity of 1×10^{14} W/cm^2 which acts as the standard candle. This allows comparison between the three detector builds.

This scaled signal eliminates the effect of the overall gain differences between the three detectors inclusive of the efficiency of the phosphor, fiber block and read out medium (film or CCD). Figure 9 contains 34 experimental data points linking the detected x-ray signal to laser intensity. Of the 34 experimental data points, 10 of the data points were used to constrain the experimental data to the simulated data at 1×10^{14} W/cm^2. The laser intensity regions above and below 1×10^{14} W/cm^2 were not constrained to follow the trend of the simulation.

The polyimide and aluminum channels are compared to the simulation results separately, giving a gain variation factor for the camera, Table 2. Comparison of the flat fielding techniques used with the witness plate results described here was reported by Benedetti et al. in RSI, 2016[28] which shows consistency of the witness plate measurements with the MCP flat fielding techniques used at NIF. The witness plate calibration experiment forms the function of both flat fielding the instrument in our experimental configuration, measuring the gain factor between the different MCP's, and providing the relationship between applied laser intensity and observed x-ray signal.

After performing this analysis the trend linking applied laser intensity and observed x-ray signal in the experiment is well reproduced by the simulation within a 10% error in x-ray signal. The range of laser intensities sampled outside of the points used for the standard can-

Detector taxon	Multiplicative Gain Factor	Gain Variation
GXD1F	160	0.5
GXD3F	99	0.9
hGXD2T	145	0.76

Table 2: The multiplicative gain factors that relate the x-ray detector signal to the simulated data shown in Figure 7. The correlation to the simulation allows a gain variation factor to be estimated which results from the gain loss as the voltage ramp moves across the strip of the detector. The error in the multiplicative gain factor and Gain variation is 10%, which reflect the experimental variation of the standard candle beam spot used to scale the data after accounting for strip to strip variation in the detectors. The x-ray detector names indicate the number of strips (T=two, F=four) and the medium which reads out the phosphor signal, GXD=CCD and HGXD=film. 'GXD' stands for gated x-ray detector

dle scaling is sufficiently large that these unconstrained data points would indicate if the simulations had not adequately linked the applied laser intensity to the expected detector response.

Determination of the error bar to match against the simulation was non trivial. The experimental results contain instrument error (pinhole size, ~10-20% is the largest factor after uncertainty in the uniformity of the gain and the statistical noise contributions in the x-ray detector totaling ~5%) additionally the x-ray transmission of the filters can vary based on the material uniformity in density and thickness (~1-2%). The results are reported with an error bar of 10% in the calculated detector response above 0.6×10^{14} W/cm^2 and 20% below this value. The RMS error of the whole data set is 22% for both filters, however we find a RMS value of 10% if we only consider the values above 0.6×10^{14} W/cm^2, reflecting higher uncertainty in the experimental points at lower laser intensities which may arise from lower absolute signal on the detector.

5. Effect of a 2:1 Laser Intensity Profile

A concern in using this method to determine the laser beam intensity profile is the accurate inference of applied laser intensities in close proximity to one another. In order to show experimentally the spatial resolution to which we can infer neighboring laser intensities we created a 2:1 laser intensity step at the calibration witness plate, shown in Figure 10. Four laser beams were overlapped at the witness plate such that there was a region of 8×10^{13} W/cm^2 where all four beams intersected neighboring a region of 4×10^{13} W/cm^2 where only two beams intersected.

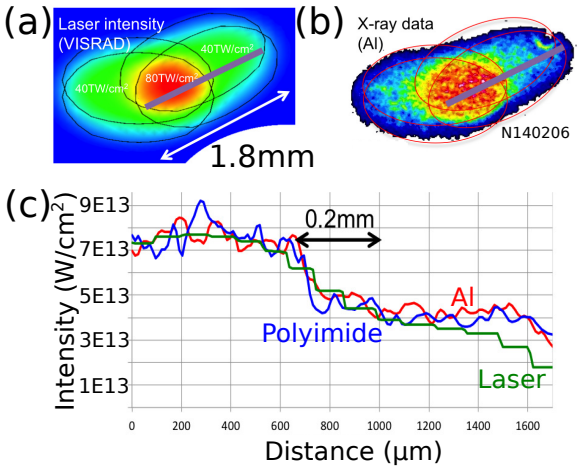

Figure 10: Four laser beams were overlapped on the witness plate to create a 2:1 intensity region. (a) shows the predicted intensity distribution from VISRAD. (b) shows the x-ray intensity distribution as seen on the Al channel. (c) The gain scaling from Figure 9 and Table 2 was applied to the x-ray data on the polyimide and Al channels and a line out is compared to the VISRAD intensity distribution (gray line on (a) and (b)) showing good agreement.

Figure 10c shows the detected x-ray intensity profile and the calculated delivered laser intensity profile from VISRAD. The x-ray image follows closely the laser intensity pattern predicted. Application of the gain factor (Table 2) for the MCP detector used and the power-law scaling, Figure 7, recovers the laser intensity 2:1 profile on both the polyimide and aluminum imaging channels. This strongly suggests that the effect of lateral heat transport at 1.3 ns is not degrading the laser intensity profile inferred from the MCP images, though this may be of concern for longer laser pulses. The combined resolution of the imaging system and the inference of the laser intensity from the witness plate is <200 μm. In order to accurately infer the applied laser intensity distribution from the x-ray image the lateral heat transport in the plate must be insignificant on the scale length of ~250 μm for the quartraum experiment.

The 2D code is severely challenged to model the experiments wherein the beams were partially overlapped to form a 2:1 intensity pattern, an inherently 3D situation. We model the system as best we can, as a rotationally symmetric 2D annulus, off axis, that has the top outer half irradiated at twice the intensity as its bottom inner half. The geometry is shown in Figure 11 where it is compared to its equivalent geometry single intensity experiment which illustrates the change in T_e and n. These simulations were for a 0.3 μm Au witness plate (on 25 μm of CH). The 2:1 case for the Ta plate is expanded in Figure 12. Comparison of Figures 12 and 11

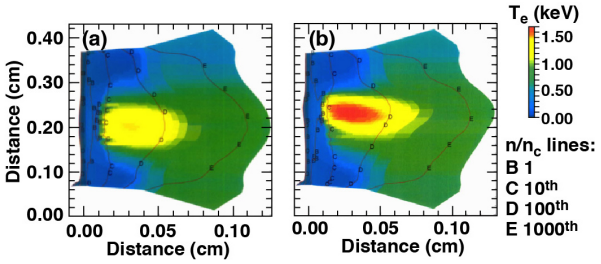

Figure 11: : Illustration of a 2:1 laser profile vs. a uniform laser profile in 2D simulation. A side view of the 2:1 Au witness plate simulation in annular 2D geometry. T_e is shown by the color map. The black line contours indicate electron density as a factor of critical density (n/n_c, 1, 0.1, 0.01) (a) shows uniform annular illumination of the witness plate, (b) shows the top half of the annulus irradiated at twice the irradiance of the bottom half. Both images are at 1.3 ns.

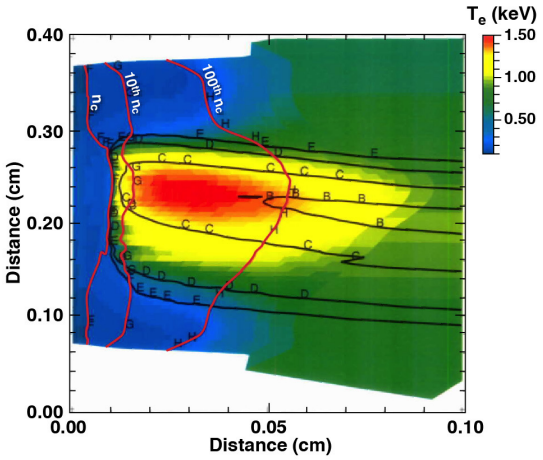

Figure 12: The 2:1 Ta witness plate shown side on. T_e color contours, red line contours of electron density, n/n_c (1, 0.1 0.01) and laser irradiance contours in black.

also highlights similar T_e distribution and density contour positions despite the change in material, this will be expanded on in the following section.

The simulations are post-processed with the appropriate experimental filter functions. Figure 13 shows a comparison of the laser intensity vs. radius and the x-ray signal. This synthetic data is produced by taking a line out in laser irradiance or emitted x-ray signal face on to the geometry shown in Figure 12. Both show a drop off from the high intensity side, and a distinct shoulder where the lower intensity laser is irradiating the witness plate. The widths are hard to compare given the compromises we have made to do an inherent 3D problem in a 2D geometry.

6. Alternate Materials for the Witness Plate

The x-ray intensity experimentally measured for a known applied laser intensity was well matched to the trend predicted in simulation for a Ta witness plate. This can give us confidence in the simulated prediction of the response from other witness plate materials. Alternate materials may already be included in an experimental target, allowing application of this described technique with little modification. Primarily they can also increase signal at the detector for a given filter combination which was the primary motivation for our inclusion of these results. To more accurately probe laser intensity below 6×10^{13} W/cm^2 we require a larger photon flux with our current microscope and detector configuration, a change in witness plate material could provide this effect.

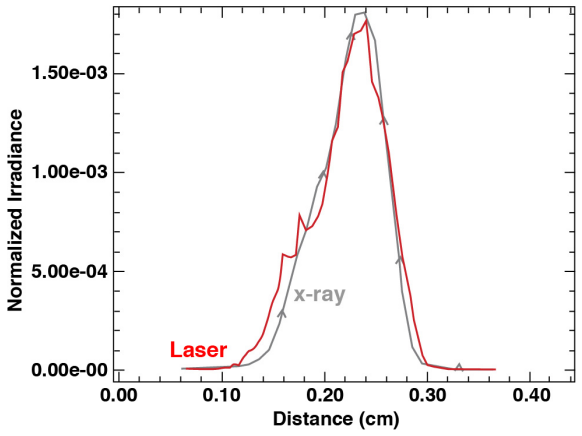

Figure 13: The normalized laser irradiance in red vs. radius and the normalized x-ray signal predicted vs. radius (grey) for the 2:1 witness plate irradiance simulations shown in Figure 12, the geometry is described in the text.

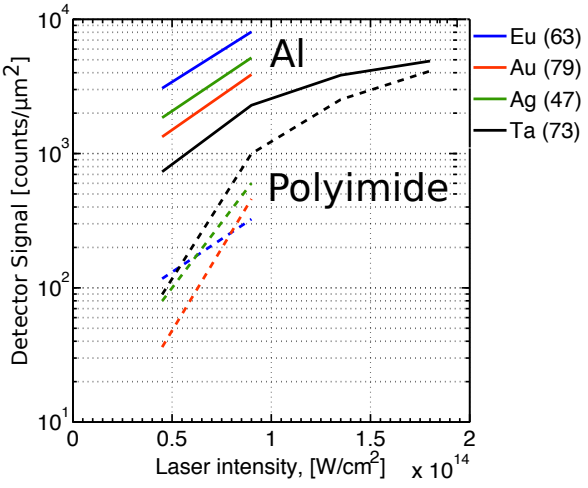

Figure 14: The simulated x-ray detector signal for four witness plate materials on the Al channel (straight lines) and polyimide channel (dashed lines) in the intensity range 5 to 10×10^{13} W/cm^2.

Figure 14 shows the simulated response of a x-ray detector with the Al and polyimide filters to alternate plate materials, Au (79) Ag (47) and Eu (63) at 4.5×10^{13} W/cm^2 and 9×10^{13} W/cm^2. All three materials increase the x-ray signal for the Al channel over a Ta (73) witness plate, with Eu showing a 4× improvement in signal at 4.5×10^{13} W/cm^2. The filters chosen for the Ta witness plate experiment suppress the n=4 to 3 transitions of M-shell emission[26] at ~2 keV (see figures 4 and 6a), by changing the material the M-shell emission energy range also shifts, this can boost the signal on the aluminum filter, Eu is particularly well matched for this reason to the Al filter used in this experiment. On the polyimide channel Au and Ag show a steep increase in x-ray signal moving from 4.5 -9$\times 10^{13}$ W/cm^2, similar to the Ta plate, the Eu emission increases more gradually. These materials may be better suited to investigating both lower and higher laser intensities than the Ta plate we have experimentally verified, depending on the sensitivity to a change in laser intensity that is needed by the experiment. Alternate detector filtering could better leverage these materials and the Ta witness plate for a specific energy range and is a point for future investigations and refinement in the experimental setup.

The Ta plate is viewed on the side of the laser interaction in the geometry described here. It may be of interest to perform a similar experiment utilizing thin wall imaging[29, 30] where a thin foil of metal is placed on a thin plastic foil and viewed on the opposite side to the laser intersection. Consideration must be made for the attenuation of the plastic and metallic material on the emitted x-rays, making this technique better suited to >5 $\times 10^{13}$ W/cm^2 intensities when combined with ~100 ps) time gated instruments.

In some cases the experimental target could be designed to allow an in situ calibration of the witness plate through the use of a calibration beam that propagates in vacuum to the surface of interest. This will allow the experimenter more freedom with diagnostic setup and filtration. To perform a successful in situ calibration of the witness plate it is vital to replicate as closely as possible the viewing angle of the plate and any x-ray or pre-pulse heating of the material. The calibration pulse should follow the same pulse shape as the beam to be diagnosed as it arrives at the surface of investigation, and ideally two to three laser intensity regions should be created in the calibration beam spot. This can also allow for other detectors not discussed here to be used such as image plate or x-ray streak cameras.

7. Conclusions

We have presented a technique that allows the laser beam intensity profile to be determined in the far field. We have extensively compared simulations and experimental results for a Ta witness plate placed at normal incidence to a beam and viewed at 45°. We will apply this technique and the resulting calibration to experiments that infer the intensity of a NIF quad after CBET has increased the intensity of the quad in a separate publication. This is of great interest to the indirect drive ICF community and also the broader research community looking at laser plasma interactions and instabilities.

The authors thank the engineering, target fabrication, and operations teams at the National Ignition Facility who made these experiments possible. This work was performed under the auspices of the U.S. Department of Energy by Lawrence Livermore National Laboratory under Contract No. DE-AC52-07NA27344 and by General Atomics under Contract DE-NA0001808. LLNL-JRNL-716802.

References

[1] A. E. Siegman, How to (maybe) measure laser beam quality, OSA TOPS 17 (1998).

[2] P. Michel, L. Divol, E. A. Williams, S. Weber, C. A. Thomas, D. A. Callahan, S. W. Haan, J. D. Salmonson, S. Dixit, D. E. Hinkel, Tuning the implosion symmetry of icf targets via controlled crossed-beam energy transfer, Physical review letters 102 (2009) 025004.

[3] J. D. Moody, P. Michel, L. Divol, R. L. Berger, E. Bond, D. K. Bradley, D. A. Callahan, E. L. Dewald, S. Dixit, M. J. Edwards, S. Glenn, A. Hamza, C. Haynam, D. E. Hinkel, N. Izumi, O. Jones, J. D. Kilkenny, R. K. Kirkwood, J. L. Kline, W. L. Kruer, G. A. Kyrala, O. L. Landen, S. LePape, J. D. Lindl, B. J. MacGowan, N. B. Meezan, A. Nikroo, M. D. Rosen, M. B. Schneider, D. J. Strozzi, L. J. Suter, C. A. Thomas, R. P. J. Town, K. Widmann, E. A. Williams, L. J. Atherton, S. H. Glenzer, E. I. Moses, Multistep redirection by cross-beam power transfer of ultrahigh-power lasers in a plasma, Nat Phys 8 (2012) 344–349.

[4] J. D. Lindl, Inertial confinement fusion: the quest for ignition and energy gain using indirect drive, American Institute Of Physics, 1998.

[5] G. H. Miller, E. I. Moses, C. R. Wuest, The national ignition facility, Optical Engineering 43 (2004) 2841–2853.

[6] D. E. Hinkel, M. B. Schneider, M. D. Rosen, E. A. Williams, The quartraum: A platform for investigation of cross-beam energy transfer, APS Meeting Abstracts 1 (2013) 7001.

[7] L. Pickworth, M. B. Schneider, D. E. Hinkel, M. D. Rosen, D. A. Callahan, P. A. Michel, A. S. Moore, J. D. Moody, Investigation of beam non-uniformity after cross-beam energy transfer in a gas filled hohlraum, Bulletin of the American Physical Society 60 (2015).

[8] T. R. Dittrich, O. A. Hurricane, D. A. Callahan, E. L. Dewald, T. Döppner, D. E. Hinkel, L. F. B. Hopkins, S. Le Pape, T. Ma, J. L. Milovich, Design of a high-foot high-adiabat icf capsule for the national ignition facility, Physical review letters 112 (2014) 055002.

[9] O. A. Hurricane, D. A. Callahan, D. T. Casey, P. M. Celliers, C. Cerjan, E. L. Dewald, T. R. Dittrich, T. Döppner, D. E. Hinkel, L. F. B. Hopkins, Fuel gain exceeding unity in an inertially confined fusion implosion, Nature 506 (2014) 343–348.

[10] R. K. Kirkwood, D. P. Turnbull, T. D. Chapman, S. C. Wilks, R. A. London, R. L. Berger, P. A. Michel, L. Divol, W. H. Dunlop, B. J. MacGowan, Initial tests of a plasma beam combiner at nif, APS Meeting Abstracts (2016).

[11] C. A. Haynam, P. J. Wegner, J. M. Auerbach, M. W. Bowers, S. N. Dixit, G. V. Erbert, G. M. Heestand, M. A. Henesian, M. R. Hermann, K. S. Jancaitis, K. R. Manes, C. D. Marshall, N. C. Mehta, J. Menapace, E. Moses, J. R. Murray, M. C. Nostrand, C. D. Orth, R. Patterson, R. A. Sacks, M. J. Shaw, M. Spaeth, S. B. Sutton, W. H. Williams, C. C. Widmayer, R. K. White, S. T. Yang, B. M. Van Wonterghem, National ignition facility laser performance status., Appl Opt 46 (2007) 3276–303.

[12] J. J. MacFarlane, Visrada 3-d view factor code and design tool for high-energy density physics experiments, Journal of Quantitative Spectroscopy and Radiative Transfer 81 (2003) 287–300.

[13] J. L. Wiza, Microchannel plate detectors, Nuclear Instruments and Methods 162 (1979) 587–601.

[14] J. A. Oertel, R. Aragonez, T. Archuleta, C. Barnes, L. Casper, V. Fatherley, T. Heinrichs, R. King, D. Landers, F. Lopez, Gated x-ray detector for the national ignition facility, Review of scientific instruments 77 (2006) 10E308.

[15] L. R. Benedetti, J. P. Holder, M. Perkins, C. G. Brown, C. S. Anderson, F. V. Allen, R. B. Petre, D. Hargrove, S. M. Glenn, N. Simanovskaia, Advances in x-ray framing cameras at the national ignition facility to improve quantitative precision in x-ray imaging, Review of Scientific Instruments 87 (2016) 023511.

[16] G. A. Rochau, J. E. Bailey, G. A. Chandler, T. J. Nash, D. S. Nielsen, G. S. Dunham, O. F. Garcia, N. R. Joseph, J. W. Keister, M. J. Madlener, Energy dependent sensitivity of microchannel plate detectors, Review of scientific instruments 77 (2006) 10E323.

[17] L. R. Benedetti, P. M. Bell, D. K. Bradley, C. G. Brown, S. M. Glenn, R. Heeter, J. P. Holder, N. Izumi, S. F. Khan, G. Lacaille, Crosstalk in x-ray framing cameras: Effect on voltage, gain, and timing (invited) a, Review of Scientific Instruments 83 (2012) 10E135.

[18] S. F. Khan, L. R. Benedetti, D. R. Hargrove, S. M. Glenn, N. Simanovskaia, J. P. Holder, M. A. Barrios, D. Hahn, S. R. Nagel, P. M. Bell, Methods for characterizing x-ray detectors for use at the national ignition facility a, Review of Scientific Instruments 83 (2012) 10E118.

[19] G. B. Zimmerman, W. L. Kruer, Numerical simulation of laser-initiated fusion, Comments Plasma Phys. Controlled Fusion 2 (1975) 51–60.

[20] H. A. Scott, S. B. Hansen, Advances in nlte modeling for integrated simulations, High Energy Density Physics 6 (2010) 39–47.

[21] G. P. Schurtz, P. D. Nicolaï, M. Busquet, A nonlocal electron conduction model for multidimensional radiation hydrodynamics codes, Physics of Plasmas (1994-present) 7 (2000) 4238–4249.

[22] M. D. Rosen, H. A. Scott, D. E. Hinkel, E. A. Williams, D. A. Callahan, R. P. J. Town, L. Divol, P. A. Michel, W. L. Kruer, L. J. Suter, The role of a detailed configuration accounting (dca) atomic physics package in explaining the energy balance in ignition-scale hohlraums, High Energy Density Physics 7 (2011) 180–190.

[23] D. E. Hinkel, M. D. Rosen, E. A. Williams, A. B. Langdon, C. H. Still, D. A. Callahan, J. D. Moody, P. A. Michel, R. P. J. Town, R. A. London, Stimulated raman scatter analyses of experiments conducted at the national ignition facility a), Physics of Plasmas (1994-present) 18 (2011) 056312.

[24] R. P. J. Town, M. D. Rosen, P. A. Michel, L. Divol, J. D. Moody, G. A. Kyrala, M. B. Schneider, J. L. Kline, C. A. Thomas, J. L. Milovich, Analysis of the national ignition facility ignition hohlraum energetics experiments a), Physics of Plasmas (1994-present) 18 (2011) 056302.

[25] H. A. Scott, C. T. Whelan, S. H. Glenzer, A study of the contribution of doubly excited ionic states to the properties of hot dense high-z plasmas, High Energy Density Physics 7 (2011) 371–376.

[26] M. Busquet, Z. Jiang, C. Y. Cote, J. C. Kieffer, M. Klapisch, A. Bar-Shalom, C. Bauche-Arnoult, A. Bachelier, Analysis of the m-shell spectra emitted by a short-pulse laser-created tantalum plasma, Physical Review E 61 (2000) 801.

[27] P. A. Baisden, L. J. Atherton, R. A. Hawley, T. A. Land, J. A. Menapace, P. E. Miller, M. J. Runkel, M. L. Spaeth, C. J. Stolz, T. I. Suratwala, Large optics for the national ignition facility, Fusion Science and Technology 69 (2016) 295–351.

[28] L. R. Benedetti, C. Trosseille, J. P. Holder, K. Piston, D. Hargrove, D. K. Bradley, P. Bell, J. Raimbourg, M. Prat, L. A. Pickworth, A comparison of flat fielding techniques for x-ray framing cameras, Review of Scientific Instruments 87 (2016) 11D622.

[29] L. J. Suter, A. R. Thiessen, F. Ze, R. Kauffman, R. H. Price, V. C. Rupert, V. W. Slivinsky, C. Wang, Use of thin wall imaging in the diagnosis of laser heated hohlraums, Review of scientific instruments 68 (1997) 838–841.

[30] E. L. Dewald, O. S. Jones, O. L. Landen, L. Suter, P. Amendt, R. E. Turner, S. Regan, Hard x-ray imaging for measuring laser absorption spatial profiles on the national ignition facility, Review of scientific instruments 77 (2006) 10E310.